Available online at www.sciencedirect.com
SCIENCE DIRECT
Journal of Catalysis 234 (2005) 328–339
JOURNAL OF CATALYSIS
www.elsevier.com/locate/jcat

Supercritical fluid removal of hydrocarbons adsorbed on wide-pore zeolite catalysts

Lucia M. Petkovic *, Daniel M. Ginosar, Kyle C. Burch

Idaho National Laboratory, P.O. Box 1625, Idaho Falls, ID 83415-2208, USA

Received 3 February 2005; revised 17 June 2005; accepted 24 June 2005

Available online 10 August 2005

Abstract

The effect of zeolite pore structure on coke removal by supercritical fluid regeneration (SFR) was studied on a series of wide-pore zeolites, including acidic Y, beta, and mordenite zeolites. Catalyst samples were deactivated under isobutane/butene reaction conditions and treated under flowing supercritical isobutane for 60 min. The chemical nature of the species remaining on the catalyst surface was analyzed by temperature-programmed oxidation, diffuse reflectance infrared Fourier transform spectroscopy (DRIFTS), and ultraviolet–visible spectroscopy. Even though most adsorbed hydrocarbons were removed in some catalysts, DRIFTS spectra indicated that none of the catalysts was completely free of hydrocarbon deposits after SFR. Cyclic reaction/SFR experiments on USY and beta zeolites showed that neither catalyst recovered its initial performance, and also demonstrated a continuous decrease in activity. However, the decrease of activity between cycles was slower in the beta sample, probably due to hindered formation of unsaturated cyclic or polycyclic compounds.

Keywords: Supercritical fluid regeneration; Isobutane/butene alkylation; Acidic zeolites; Coke analysis; FAU; BEA; MOR

1. Introduction

The introduction of acidic zeolites to replace the liquid acid catalysts used in isobutane/butene alkylation processes has long been sought, but because zeolite catalysts deactivate rapidly due to coke deposition and can be oxidatively regenerated only a few times precludes the commercial application of these catalysts [1]. To improve solid acid catalyst lifetime and decrease coke precursor deposition, alkylation under near-critical and supercritical conditions has been considered [2–7]. Ginosar et al. [6] reported that the addition of supercritical cosolvents did not result in sustained catalytic alkylation activity at industrially relevant conditions; however, they found that deactivated alkylation catalysts could be successfully regenerated with supercritical isobutane. They showed that partially deactivated catalysts could be completely regenerated [8,9] and demonstrated that catalyst activity and product yields scarcely decreased after 23 reaction/regeneration cycles, remaining at 100% of initial activity over the entire course of their experiment. Fully deactivated catalysts recovered as much as 82% of the fresh catalyst activity [10].

Petkovic and Ginosar [11] demonstrated that regardless of deactivation level, a USY zeolite catalyst submitted to supercritical fluid regeneration (SFR) recovered most of its initial micropore volume. However, samples that were allowed to reach high levels of deactivation contained coke precursors that were further dehydrogenated, condensed, and eventually not extracted during the SFR treatment. These condensed compounds were proposed as the cause of the lower catalyst activity recovery of fully deactivated catalysts by SFR [12].

For the research work presented in this contribution, we hypothesized that the open pore structure of the USY zeolite may have played a role in facilitating hydrocarbon cyclization reactions, which decreased SFR effectiveness. It is known that both zeolite pore structure and acidity affect the amount, nature, and location of coke precursors in catalytic

* Corresponding author. Fax: +1-208-526-8541.
E-mail address: petklm@inel.gov (L.M. Petkovic).

0021-9517/$ – see front matter
doi:10.1016/j.jcat.2005.06.027

hydrocarbon conversions [13], but how those properties influence the removal of hydrocarbons by SFR treatment has not been reported thus far. To understand the effect of zeolite pore structure on coke removal by SFR, a series of 12 member-ring (MR) zeolite catalysts displaying a variety of pore structures and acid site densities was deactivated under a flowing isobutane/butene mixture and then submitted to SFR. Catalyst samples, including acidic Y, beta, and mordenite zeolites, were deactivated under liquid phase isobutane/butene reaction at 333 K and 1.1×10^7 Pa for 360 min and submitted to SFR under flowing supercritical isobutane at 453 K and 1.1×10^7 Pa for 60 min. Samples of Y and beta zeolites displaying different SiO_2/Al_2O_3 ratios were used to differentiate the effects of pore structure from acid site density on coke precursor formation and removal. The chemical nature of the species remaining on the catalyst surface before and after SFR was analyzed by temperature-programmed oxidation (TPO), diffuse reflectance infrared Fourier transform spectroscopy (DRIFTS), and ultraviolet–visible (UV–vis) spectroscopy.

2. Experimental

All catalyst precursors used in this study were commercially available forms of zeolite purchased from Zeolyst (Valley Forge, PA). Y zeolite catalyst precursors were CBV 712 and CBV 720. Beta zeolite catalyst precursors were CP 814N and CP 814E. The mordenite catalyst precursor was CBV 21A. All were received in powdered form without binders, and all but CBV 720, which was in hydrogen form, were received in ammonium form. A summary of the zeolite samples and their SiO_2/Al_2O_3 ratios is given in Table 1.

All samples were palletized, crushed, and sieved, and the fraction between 8 and 20 ASTM mesh was collected and calcined at 823 K for 3 h to obtain the acid form of the catalyst. The CBV 720 sample was calcined for 1 h at 823 K.

The nomenclature used in this contribution is shown in Table 1. The nomenclature may also include an F, S, or R as a suffix for fresh, spent (i.e., after reaction and before SFR), and after SFR samples, respectively. For example, B18F represents the fresh acid form of the catalyst prepared using the CP 814N zeolite as catalyst precursor, B18S is the deactivated catalyst, and B18R is the sample after SFR.

Both the continuous flow reaction/SFR treatment experimental system and the general operating procedure used in this study are described in detail elsewhere [10,11]. In brief, the experimental system consisted of a stainless steel tube reactor (44 cm long × 8 mm i.d.), high-pressure syringe pumps, a recycle pump, and an on-line gas chromatograph (GC). For the reaction step, the reactor was operated in partial recycle mode, whereas the SFR step was operated in a single pass mode.

Table 1
Zeolite samples utilized in this study

Sample nomenclature	Y12	Y30	B18	B25	M20
Precursor	CBV 712	CBV 720	CP 814N	CP 814E	CBV 21A
SiO_2/Al_2O_3[a]	12	30	18	25	20

[a] Reported by manufacturer.

The reactant mixture consisted of a premixed isoparaffin:olefin (iP:O) molar ratio 20:1 of isobutane/2-butene (Praxair) feed, for the reaction step. A typical fresh feed molar composition as determined by GC analysis was 94.75% isobutene, 2.83% *trans*-2-butene, and 2.06% *cis*-2-butene. The only impurities detected were propane (0.20%) and *n*-butane (0.16%). Fresh feed and recycle flow rates were 2.5 and 50 cm^3/min, respectively. Isobutane (99.48%; Praxair) was used both for pressurizing the system before reaction and for the SFR treatment. Impurities in the isobutane stream were propane (0.23%) and *n*-butane (0.29%).

Two experiments were performed with each catalyst sample. The first experiment consisted of a liquid phase isobutane/butene reaction to deactivate the catalyst; the second, of reaction followed by SFR treatment. For each experiment, 8 g of the dried acid form of the catalyst were loaded in the reactor and pretreated overnight in situ at 473 K under flowing helium. The temperature was then decreased to 333 K, and the system was pressurized at 1.1×10^7 Pa with isobutane. At time zero, the flow of reactant mixture (i.e., isobutane/2-butene feed) was initiated at a flow rate necessary to achieve an olefin weight hourly space velocity (OWHSV) of 0.5 g butene/(g_{cat} h). Samples of the product stream during reaction were analyzed automatically every 20 min using a Hewlett Packard 5890 Series II gas chromatograph operated under the same conditions as reported previously [11]. The experimental setup did not allow for product stream sampling during SFR treatment.

For the reaction-only experiments, the reactant mixture flow was stopped after 360 min time- on-stream (TOS), the system was cooled to room temperature and flushed with helium at 3.4×10^6 Pa for 2 h, and the catalyst was recovered. These samples were assumed to represent the catalyst conditions after reaction and before SFR.

For the reaction/SFR experiments, the reactant flow was stopped after 360 min TOS, and 2 ml/min of isobutane at 1.1×10^7 Pa was flowed through the reactor. The temperature was increased to 453 K over a period of 30 min to achieve supercritical conditions and kept at 453 K for 60 min. Finally, the system was cooled and flushed, and the catalyst was recovered following the same procedure as described for the reaction-only experiments. The samples were immediately stored in closed containers to minimize contact with environmental moisture.

For cyclic reaction/SFR regeneration experiments, the experimental setup was modified to accommodate two reactors operated in swing mode. Eight grams of zeolite catalysts were loaded in each reactor and submitted to four 360-min reaction/60-min SFR cycles. While one reactor was operated under reaction conditions for 360 min, the other reactor was either operated under 60 min of SFR treatment or held in

liquid isobutane under reaction conditions waiting for completion of 360 min before starting the next reaction cycle.

Nitrogen physisorption and ammonia chemisorption measurements were performed on an automated Quantachrome Autosorb-1C system. To minimize changes in the amount and nature of carbonaceous species retained on the catalyst surface, the pretreatment of spent and SFR treated samples for nitrogen physisorption measurements consisted simply of outgassing at 298 K for 3 h. For fresh catalyst samples, zeolite precursors (either ammonium or hydrogen form) were calcined at 823 K under flowing air for either 1 or 3 h, kept overnight at 473 K under flowing helium, and outgassed at 473 K for 3 h. Then the samples were weighed and the nitrogen physisorption measurements started. BET [14] surface areas (SAs) were calculated in the P/P_0 range of 0.05–0.10, and micropore volume (MPV) was determined by the t-plot method [15].

Acid site density by ammonia chemisorption was determined at 448 K by the bracketing method, which involves measuring two adsorption isotherms. The first isotherm, the so-called "combined" isotherm, reflects the total amount of ammonia adsorbed at a given temperature, which accounts for both strongly and weakly adsorbed molecules. To measure the second isotherm, the system is first evacuated to desorb the weakly adsorbed molecules, and a new round of ammonia doses is used to quantify those sites. This second isotherm, the so-called "weak" isotherm, accounts for the weakly adsorbed ammonia molecules. The difference between both isotherms is a measure of the number of acid sites capable of strongly chemisorbing ammonia at 448 K. This number of strong acid sites is adopted in this paper as a measure of the acid site density of the sample. Fresh catalyst samples were submitted in situ to the same protocol as that applied for nitrogen physisorption measurements on fresh samples. After 3 h of evacuation at 473 K, the temperature was decreased to 448 K, and the automated capabilities of the sorptometer were used to measure the combined and weak isotherms.

The content of hydrocarbons deposited on the catalysts was determined by temperature-programmed oxidation (TPO) on a Perkin–Elmer Diamond TG/DTA microbalance under 100 ml/min flowing air. Typically, 10 mg of sample was placed in the balance pan and heated at 10 K/min from room temperature to 373 K. The temperature was kept at 373 K for 30 min, increased to 1073 K at 10 K/min, and then decreased to 373 K and kept there for 1 h. The changes in weight between the reading at the end of the initial step at 373 K and the final step at 373 K were recorded to calculate hydrocarbon content. The negative of the derivative of the weight changes with respect to time revealed two peaks. The mass percentage corresponding to each of these peaks was calculated from the area under the peak between 373 and 673 K for the first peak and between 673 and 1073 K for the second peak. To account for any contribution of water to the weight changes in the thermogravimetric analysis, a set of blanks experiments was performed by submitting fresh catalyst samples to the same protocol as the rest of the samples and up to the point of pressurization with isobutene. The TPO weight changes of the blank samples were subtracted from the weight changes corresponding to spent and SFR-treated samples.

DRIFTS studies were performed at room temperature on a Nicolet Magna 750 Fourier transform infrared spectrometer equipped with a commercial Spectratech diffuse reflectance cell. A total of 800 scan spectra were collected in the 4000–400 cm^{-1} range at a resolution of 4 cm^{-1}.

UV–vis diffuse reflectance spectroscopy measurements were done with a Shimadzu UV-3101 PC scanning spectrophotometer equipped with an integrating sphere attachment. A small amount of powder catalyst sample was placed on paper, and spectra were collected in the 700–250 nm wavelength range. All DRIFTS and UV–vis spectra are shown off-set for clarity.

3. Results

3.1. Catalyst deactivation

To better understand the effect of zeolite pore structure on the removal of coke deposits by SFR treatment, the effect of zeolite pore structure on coke deposition (and hence on catalyst deactivation) must be analyzed. Catalyst activity profiles show the macroscopic result of complex chemical reactions that occur within the zeolite channels and that produce both fluid products and undesired hydrocarbon deposits.

Catalyst activity as measured by butene conversion is shown on Fig. 1. All catalyst samples showed deactivation with TOS. The so-called "useful catalyst lifetime" proposed by Taylor and Sherwood [16], characterized by high olefin conversion and slow catalyst deactivation, ranged between ca. 60 min for B18 and nearly absence (immediate deac-

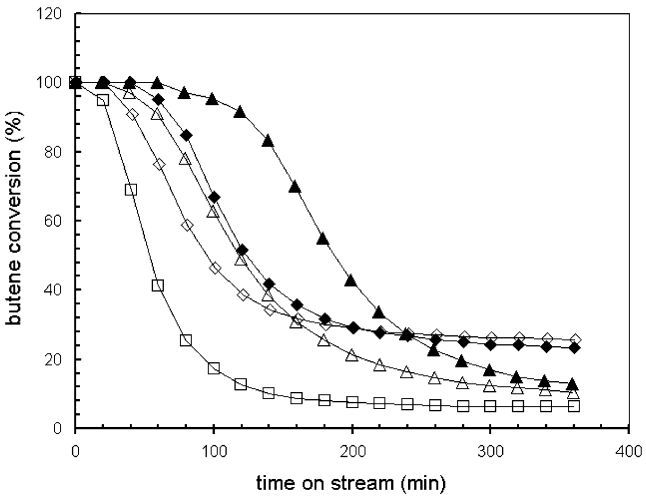

Fig. 1. Catalyst activity as measured by butene conversion. Samples are Y12 (◆), Y30 (◇), B18 (▲), B25 (△), and M20 (□) zeolite catalysts.

Table 2
Physical properties of the catalyst samples

Sample	Acidity[a] (μmol/g)	SA (m^2/g)	MPV (cm^3/g)	Sample	SA (m^2/g)	MPV (cm^3/g)	MPV[b] (%)	Sample	SA (m^2/g)	MPV (cm^3/g)	MPV[b] (%)
Y12F	509	747	0.24	Y12S	467	0.16	67	Y12R	652	0.23	96
Y30F	213	865	0.27	Y30S	753	0.22	81	Y30R	848	0.26	96
B18F	741	628	0.19	B18S	204	0.00	0	B18R	477	0.10	53
B25F	345	671	0.17	B25S	186	0.03	18	B25R	252	0.03	18
M20F	642	523	0.18	M20S	44	0.00	0	M20R	111	0.02	11

[a] Determined by bracketing method.
[b] Percentage MPV defined as MPV/(fresh MPV) × 100.

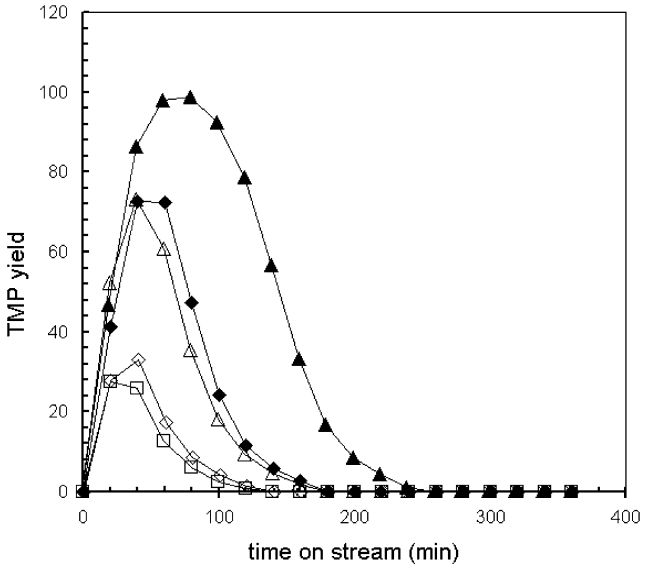

Fig. 2. Trimethylpentane yield. TMP yield is defined as grams of TMP/(gram of butene in feed) × 100. Samples are Y12 (◆), Y30 (◇), B18 (▲), B25 (△), and M20 (□) zeolite catalysts.

tivation) for M20. The order of decreasing useful catalyst lifetimes was B18 > Y12 > B25 > Y30 > M20.

During the useful catalyst lifetime, butene was completely converted. Beyond the useful catalyst lifetime, catalysts entered the rapid deactivation stage, in which a pronounced decreased in activity along with a change in selectivity to C_{9+} products was evident. Even at short TOS, the conversion of butene on M20 was not complete, and this catalyst showed marked deactivation from the beginning of the experiment. During the final stage, catalyst deactivation was again slow, and fluid products were primarily C_{9+} products.

Maximum total product yields to C_{5+} products as percent of butene in feed were 146% for B18, 127% for Y12, 108% for B25, 64% for Y30, and 35% for M20. Trimethylpentane (TMP) yields are shown in Fig. 2. Because GC analyses could not discriminate 2,2,3-trimethylpentane from 2,5-dimethylhexane, the TMP yields shown in Fig. 2 account only for 2,2,4-, 2,3,4-, and 2,3,3-trimethylpentanes. The order of TMP production was B18 > Y12 ≈ B25 > Y30 ≈ M20.

These results demonstrate that total product yields with respect to butene were much lower than the expected from a system working under true alkylation conditions. In fact, a large portion of the saturated hydrocarbons in the product stream was likely produced by butene dimerization with hydride transfer. Moreover, a decrease in hydrogen transfer rate with TOS lead to enhanced oligomerization and formation of heavier hydrocarbons that eventually deactivated the catalysts completely.

3.2. Catalyst physical properties

Catalyst physical properties are summarized in Table 2. Comparing surface area and MPV of spent samples with the corresponding fresh catalysts, it is easily seen that surface areas and MPV were lower after reaction, as expected. Y zeolite catalysts conserved an important portion of their initial MPV after reaction, but the rest of the catalysts showed significant MPV decrease. By submitting the spent catalysts to SFR, both Y zeolite catalysts recovered almost all of their initial MPV. For B18, the recovery of MPV was around 53%. The recovery of MPV was very small on M20, and no recovery was found on B25.

3.3. Characterization of adsorbed hydrocarbons

3.3.1. TPO experiments

TPO was used to measure the amount of hydrocarbons remaining on the catalysts before and after SFR. Most TPO profiles presented two peaks, one produced by desorption of a portion of hydrocarbon species retained in the catalyst pores and the other produced by oxidation of the remaining hydrocarbons to CO_2 [11]. A summary of the amount of hydrocarbons desorbed and peak maximum temperatures is given in Table 3. Relatively small amounts (3.9 and 1.4%) of hydrocarbons were adsorbed on the Y catalyst samples after reaction. An intermediate amount (5.9%) was found on spent mordenite, and the highest amounts (11.5 and 10.0%) were found on spent beta zeolite catalysts. The SFR produced almost complete removal of hydrocarbons from both spent Y zeolite catalysts. With respect to beta zeolite samples, about 77% was removed from B18S, but only 16% from B25S. From mordenite, 46% of was removed.

The temperatures at which the first TPO peak reached its maximum were between 459 and 524 K before SFR and between 431 and 509 K after SFR. The temperatures for the

Table 3
Temperature-programmed oxidation of hydrocarbons deposited on zeolite catalyst samples before and after SFR

Sample	1st peak		2nd peak		Total (wt%)	Sample	1st peak		2nd peak		Total (wt%)
	wt%	T (K)	wt%	T (K)			wt%	T (K)	wt%	T (K)	
Y12S	1.1	490	2.8	794	3.9	Y12R	0.0	–	0.0	–	0.0
Y30S	0.3	503	1.1	794	1.4	Y30R	0.0	–	0.1	784	0.1
B18S	5.5	476	6.0	783	11.5	B18R	0.7	431	1.9	763	2.6
B25S	5.7	524	4.3	792	10.0	B25R	4.6	509	3.8	793	8.4
M20S	3.2	459	2.7	804	5.9	M20R	1.7	456	1.5	795	3.2

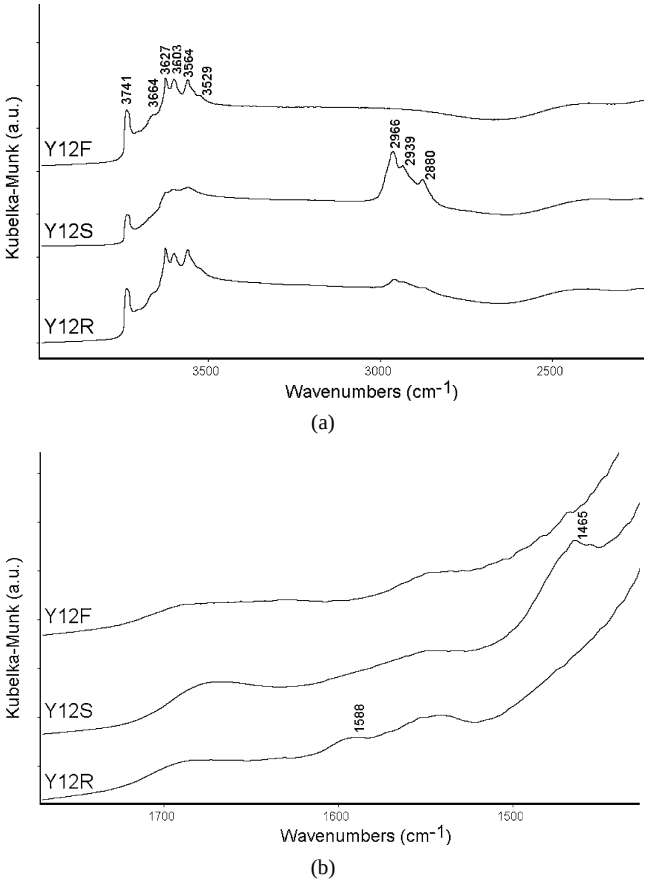

Fig. 3. DRIFTS spectra of Y12 catalyst samples in the CH and OH stretching (a) and CC stretching and CH deformation (b) region.

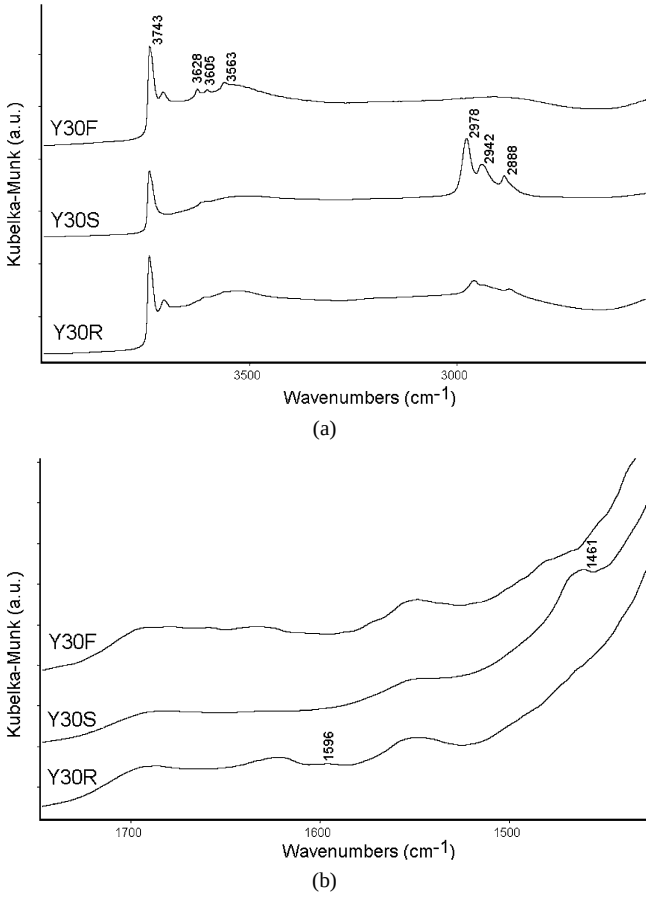

Fig. 4. DRIFTS spectra of Y30 catalyst samples in the CH and OH stretching (a) and CC stretching and CH deformation (b) region.

second TPO peak were between 783 and 804 K before and 763 and 795 K after SFR. The highest first peak temperatures corresponded to B25 samples (i.e., B25S and B25R); the highest second peak temperatures, to M20 samples (i.e., M20S and M20R).

3.3.2. DRIFTS

Figs. 3–7 show the DRIFTS spectra of samples fresh, before, and after SFR. For hydrocarbons species, bands from 2700 to 3100 cm^{-1} correspond to CH stretching vibrations, and bands at or below 1650 and 1465 cm^{-1} correspond to CC stretching and CH deformation vibrations, respectively [17]. For zeolites, peaks around 3745 cm^{-1} are usually assigned to external terminal silanol groups, peaks around 3600–3500 cm^{-1} are assigned to hydroxyl groups of the internal zeolite surface [18,19], and peaks below ∼1500 cm^{-1} [20] are assigned to skeletal vibrations of the zeolite structure. Although bands around 1635 cm^{-1} may be assigned to C=C stretching [17], water also absorbs infrared radiation around that frequency and produces a typical deformation band when adsorbed on zeolite materials [21]. Hence, we do not consider bands around 1635 cm^{-1} in the analysis that follows.

Fig. 3 shows the DRIFTS spectra of the Y12 zeolite catalyst samples. The fresh sample (Y12F) revealed the silanol peak at 3741 cm^{-1} and a multiplicity of hydroxyl peaks between 3664 and 3529 cm^{-1} (Fig. 3a). From literature assignments [22], Y zeolite OH bands at 3627 and 3564 cm^{-1} correspond to bridged Si–OH–Al in supercavi-

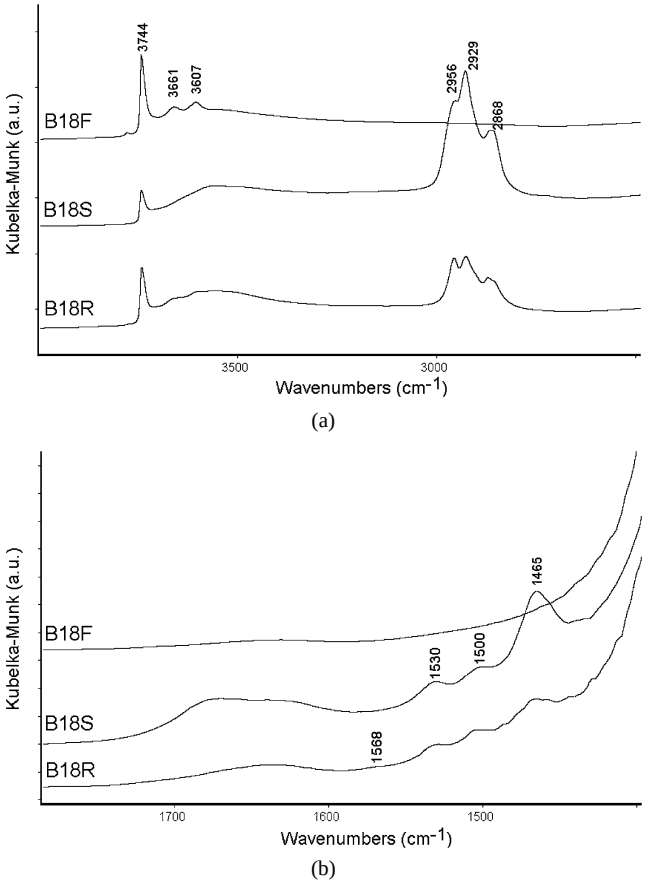

Fig. 5. DRIFTS spectra of B18 catalyst samples in the CH and OH stretching (a) and CC stretching and CH deformation (b) region.

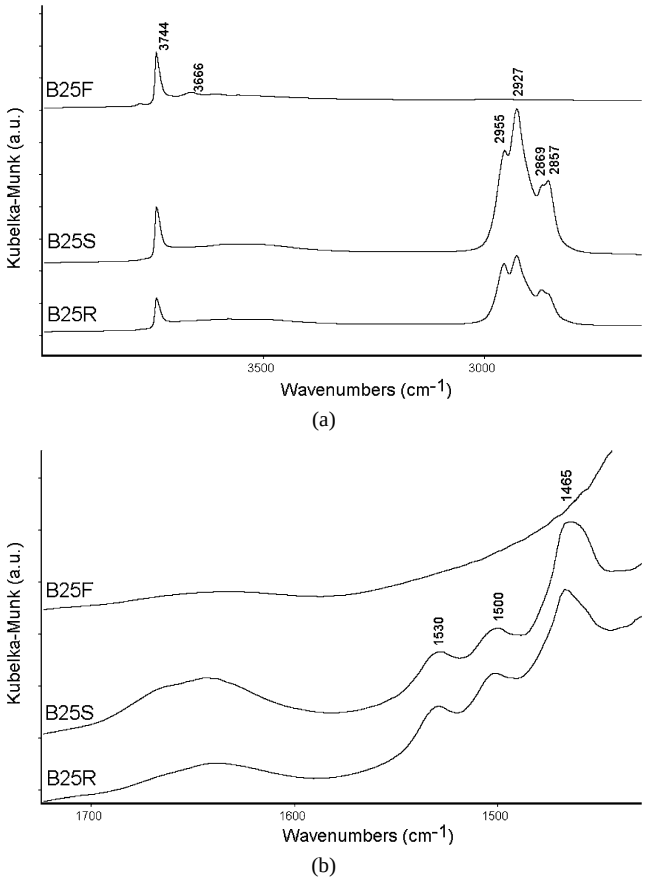

Fig. 6. DRIFTS spectra of B25 catalyst samples in the CH and OH stretching (a) and CC stretching and CH deformation (b) region.

ties and hexagonal prisms, respectively. The Y12S spectrum (Fig. 3a) showed decreased intensity on the hydroxyl region and displayed aliphatic CH stretching bands between 2800 and 3000 cm^{-1}, in which the contribution of the $\nu_{as}CH_3$ peak at 2966 cm^{-1} was relatively important with respect to the contribution of $\nu_{as}CH_2$ at 2939 cm^{-1}. On the Y12R spectrum, the CH stretching bands showed decreased intensity, and the OH region recovered the features of the Y12F sample.

Comparing the spectra of fresh (Y12F) and spent (Y12S) samples on Fig. 3b, a band around 1465 cm^{-1} usually assigned to CH deformation of CH_3 groups is noticeable on the Y12S spectrum. On the spectrum after SFR (Y12R), the band at 1465 cm^{-1} is absent, and a band at 1588 cm^{-1} is apparent. Bands around 1580–1610 cm^{-1} are usually assigned to complex mixtures of hydrogen-deficient carbonaceous deposits [23].

Fig. 4 shows the DRIFTS spectra of Y30 zeolite catalysts. Most of the bands seen on this set of spectra resemble those seen on the Y12 catalysts. Whereas on the Y30R spectrum the CH stretching bands showed decreased intensity, the hydroxyl region did not recover all of the features of the Y30F sample.

Fig. 5 shows the DRIFTS spectra of B18 zeolite catalyst samples. In Fig. 5a, curve B18F, the silanol peak is at 3744 cm^{-1} and hydroxyl peaks are at 3661 and 3607 cm^{-1}, which may be assigned to extra-framework alumina species and Brønsted acid sites [24], respectively. The B18S spectrum displayed CH stretching bands in which the contribution of the $\nu_{as}CH_2$ (aliphatic) at 2929 cm^{-1} was relatively important with respect to the contribution of $\nu_{as}CH_3$ peak at 2956 cm^{-1}. On the B18R spectrum, the relative contribution of the $\nu_{as}CH_3$ peak at 2956 cm^{-1} increased. In Fig. 5b, a CH deformation band at 1465 cm^{-1} and bands at 1500 and 1530 cm^{-1} are seen on B18S and with lower intensity on B18R. The latter two bands, which have been assigned in the literature to alkenyl carbocations [25,26], have also been observed by Feller et al. [27] on spent H-beta alkylation catalysts. Throughout this paper, we use the term “carbocation” in a loose sense; “surface alkoxides” may be a more accurate term for these active hydrocarbon species adsorbed on acidic zeolite surfaces.

Fig. 6 shows the DRIFTS spectra of B30 beta zeolite catalyst samples. These spectra resemble those obtained from B18 samples. However, the intensities of the CH deformation bands before (B25S) and after SFR (B25R) were comparable.

Fig. 7 shows the DRIFTS spectra of M20 zeolite catalysts. The silanol peak was at 3745 cm^{-1}, and hydroxyl peaks were around 3659 cm^{-1}. The aliphatic CH stretch-

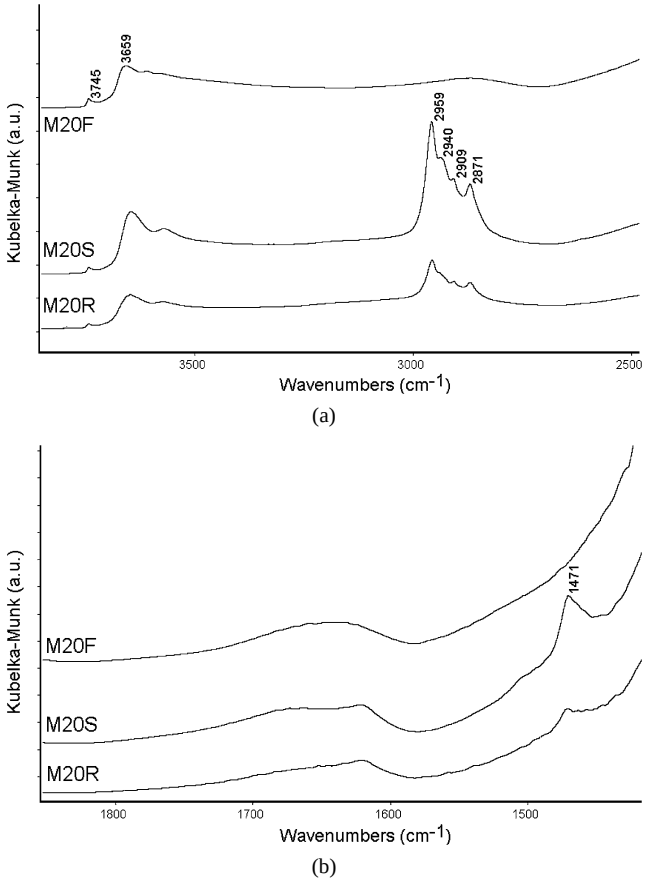

Fig. 7. DRIFTS spectra of M20 catalyst samples in the CH and OH stretching (a) and CC stretching and CH deformation (b) region.

ing bands between 2800 and 3000 cm^{-1} showed decreased intensity after SFR (i.e., the M20R sample). The contribution of the $\nu_{as}CH_3$ peak at 2959 cm^{-1} was important both before and after SFR. In Fig. 7b, a CH deformation band at 1471 cm^{-1} is seen on the M20S spectrum and with decreased intensity on the M20R spectrum as well.

3.3.3. UV–vis

UV–vis diffuse reflectance absorption spectra are shown in Figs. 8–12. UV–vis bands between 290 and 345, 370 and 390, and 430 and 490 nm are assigned to allylic, dienylic, and polyenylic carbocations, respectively [26,28–32]. Bands around 410 nm have been reported to arise from a number of unsaturated cyclic structures, including diphenyl carbocations, alkylaromatics, polyaromatics [33], and polycyclic aromatic compounds [29].

Fig. 8 shows the UV–vis spectra of the Y12 samples. Before SFR (i.e., Y12S curve), monoenylic (320 nm) and dienylic (381 nm) carbocations were detected. After SFR, a broad band at 429 nm assigned to unsaturated cyclic compounds was apparent.

Fig. 9 shows the UV–vis spectra of the Y30 samples. Only after SFR (i.e., Y30R curve) was a noticeable absorption assigned to unsaturated cyclic compounds observed.

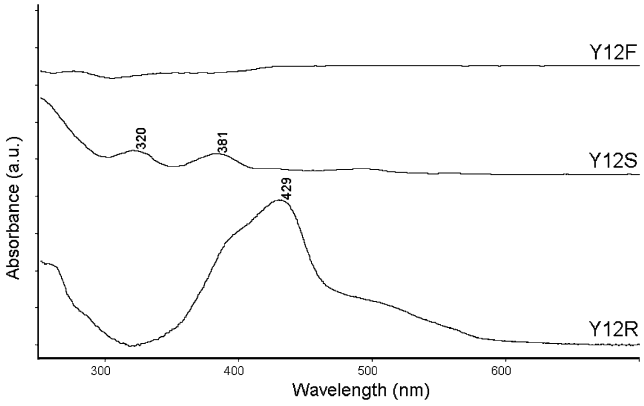

Fig. 8. UV–vis spectra of Y12 catalyst samples.

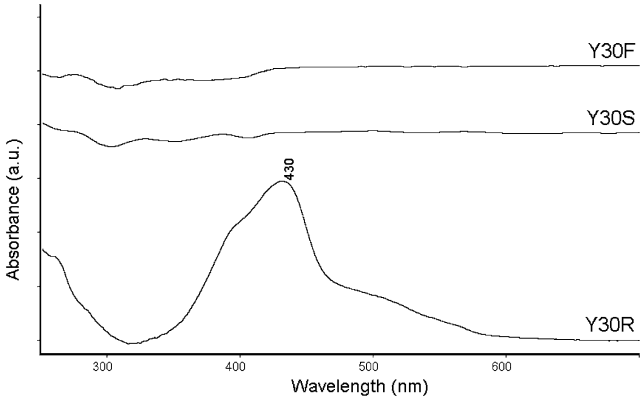

Fig. 9. UV–vis spectra of Y30 catalyst samples.

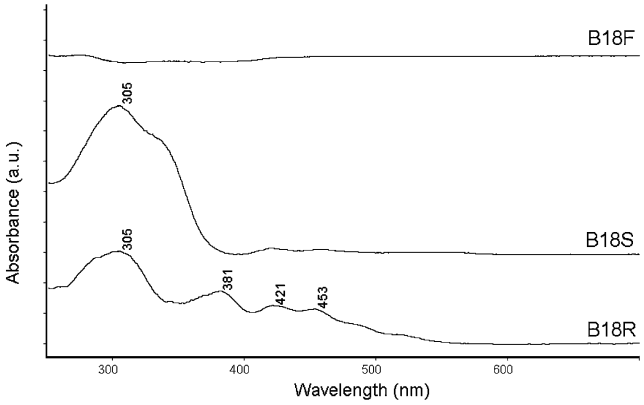

Fig. 10. UV–vis spectra of B18 catalyst samples.

Fig. 10 shows the UV–vis spectra of the B18 samples. The spent sample (B18S) displayed absorption around 305 nm, which corresponds to allylic carbocations. After SFR (i.e., curve B25R) the presence of these species was still noticeable, along with species of more elevated degree of unsaturation that absorbed around 381 nm and higher wavelengths.

Fig. 11 shows the UV–vis spectra of the B25 samples. The main contribution to UV–vis absorption arose from species with low degrees of unsaturation both before and after SFR.

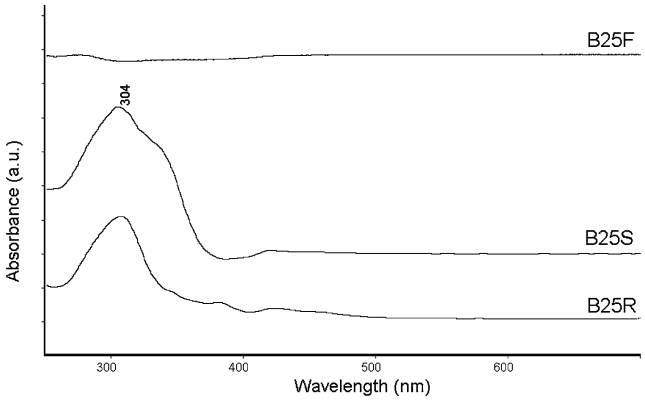

Fig. 11. UV–vis spectra of B25 catalyst samples.

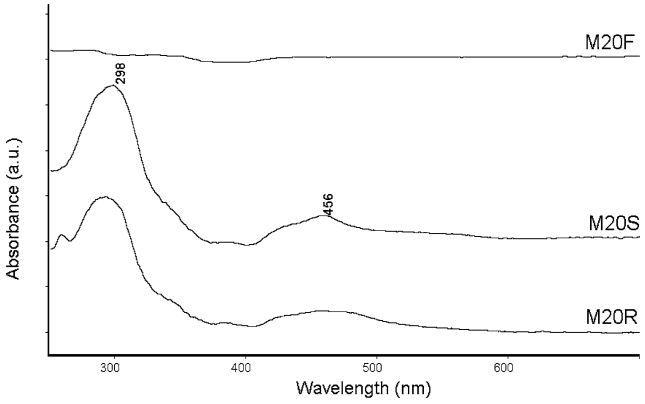

Fig. 12. UV–vis spectra of M20 catalyst samples.

Fig. 12 shows the UV–vis spectra of the M20 samples. Both before and after SFR, the M20 samples displayed absorption around 298 nm, which corresponds to allylic carbocations, and around 456 nm, which may be assigned to polyenylic carbocations.

3.4. Cyclic reaction/SFR experiments

Recovery of catalyst activity by SFR treatment was tested on the B18 catalyst and on the USY (SiO_2/Al_2O_3: 5.2) catalyst studied previously [11]. The USY catalyst was selected because its activity profile did not differ much from the activity profile of the B18 sample and yet the type of hydrocarbons remaining on its surface after SFR presented a significant contribution of polycyclic aromatic compounds absorbing infrared radiation at 1580 cm^{-1} and UV–vis at 425 nm [11]. In contrast, the B18 sample did not show a significant contribution of those species after SFR treatment, as seen in Figs. 5 and 10.

Integrated conversions, C_{5+} yields, and TMP yields may be used as measures of catalyst activity and selectivity. These values were estimated by integrating the TOS curves of conversion, C_{5+} yield, and TMP yield. An integrated conversion of 100% implies that all butene that entered the reactor (i.e., 24 g/cycle) was converted to products. If all butene were converted to TMPs, then the expected integrated TMP yield would be about 203% (e.g., 114 g TMP produced/56 g butene consumed).

Comparing the two catalysts, the activity and TMP yield were relatively higher on USY at the beginning of the experiment (see Table 4). Activity decreased each subsequent cycle, and during the fourth reaction cycle, B18 displayed an average of 68% of its initial (i.e., first cycle) integrated conversion; USY, an average of 50%.

TMP yields also decreased on both catalysts, but the decrease was more pronounced on USY. It is noteworthy that the most important decrease in activity and TMP yield occurred between the first and second cycles. From the second to fourth cycles, the rate of activity and TMP yield loss was less marked, and B18 behavior was relatively more stable.

4. Discussion

4.1. Hydrocarbon deposition

Both catalyst activities (Fig. 1) and trimethylpentane yields (Fig. 2) were highest on B18 and lowest on M20 zeolite catalysts. The trend of decreasing activity was approximately B18 > Y12 > B25 > Y30 > M20. When correlating catalyst acid site density (Table 2) with both activity and TMP yield, a direct correlation was found for the zeolite catalysts having three-dimensional (3D) pore structures. Faster deactivation and decreased TMP selectivity with increased SiO_2/Al_2O_3 ratio on Y zeolite alkylation catalysts has also been reported by Yoo et al. [34]. These authors observed a monotonic increase in deactivation with an increase in SiO_2/Al_2O_3 ratio at low temperatures, in contrast with the behavior observed on zeolite catalysts at elevated temperatures, with improved tolerance to coking with increasing

Table 4
Integrated conversions and TMP yields for 4 consecutive reaction/SFR cycles

	Integrated conversion (% butene converted)				Integrated C_{5+} yield (% butene in feed)				Integrated TMP yield (% butene in feed)			
Sample	B18		USY		B18		USY		B18		USY	
Reactor	1	2	1	2	1	2	1	2	1	2	1	2
1st cycle	67	52	73	64	55	34	90	85	32	17	54	45
2nd cycle	48	47	43	49	28	28	33	45	13	13	15	22
3rd cycle	49	43	40	40	28	24	25	15	12	10	9	10
4th cycle	43	38	34	35	27	20	16	16	13	9	5	4

SiO_2/Al_2O_3 ratio. The increase of activity and TMP selectivity with aluminum content is explained by the improvement in hydrogen transfer reactions that allow for desorption of TMPs+ and other adsorbed hydrocarbons that may eventually deactivate catalyst active sites [34].

For a given 3D pore structure, the lower the acid site density (Table 2), the lower the amount of hydrocarbons retained during reaction (Table 3). Even though the hydrocarbon content was lower, the temperature at which those hydrocarbons desorbed during the TPO experiments was higher. Theoretical considerations have demonstrated an increase in acid site strength with decreasing aluminum content of the zeolite framework [35]. In other words, although the acid site density of 12-member-ring zeolites increases as the aluminum concentration in the lattice increases, the acid strength of specific sites may decrease because of decreasing framework electronegativity as Si atoms are replaced by Al atoms [36]. This may explain the higher temperatures needed to desorb hydrocarbons from Y30S and B25S with respect to Y12S and B25S, indicating that those hydrocarbons were probably more tightly bound to the catalyst surface due to the stronger acidity of particular sites.

Although the activity (Fig. 1) and TMP (Fig. 2) profiles of the Y12 and B25 samples did not differ much, their hydrocarbon content (Table 3) and MPV available after reaction (Table 2) were markedly different. More stable zeolite alkylation catalysts have been reported to retain higher amounts of hydrocarbons [34,37]. From the results presented here, higher hydrocarbon content was found on more active samples only when comparing catalysts within a given pore structure (i.e., Y12S vs. Y30S, or B18S vs. B25S). This trend is also confirmed when comparing Y12S and Y30S with the USY catalyst reported previously [11]. The USY was more active than the Y12S, and its hydrocarbon content reached 16.3%. In addition, the trend in hydrocarbon content for USY, Y12, and Y30 samples is proportional to the acid site density of those three samples. Different mechanisms for catalyst deactivation by coke deposition have clearly taken place on zeolite catalysts of different pore structures.

Feller et al. [27] found that a spent beta zeolite alkylation catalyst contained pores completely filled with alkanes, aromatics, and highly unsaturated and branched polymers, similar to the conjunct polymers formed under liquid acid catalytic alkylation. Although alkanes were shown by DRIFTS on both spent beta catalysts studied here, neither aromatic CH stretching above 3000 cm^{-1} nor condensed hydrocarbon bands around 1580 cm^{-1} were found.

The relatively high MPV found on spent Y zeolite catalysts (Y12S and Y30S in Table 2) may explain the higher final butene conversion (Fig. 1) to fluid products because the diffusion of fluid products out of the catalyst micropores was less constrained by hydrocarbon deposits. An almost linear correlation between hydrocarbon content and MPV decrease was found for all of the spent zeolite catalysts with 3D pore structures studied here. Similar behavior has been reported in the literature for cation-exchanged Y zeolite [38] and for USY alkylation catalysts submitted to different TOS [11]. But this trend is not maintained when the mordenite catalyst is included. For example, 5.9% of hydrocarbon deposits brought mordenite to display negligible MPV, whereas 10.0% of hydrocarbon deposits allowed B25S to still display 0.03 cm^3/g. A pore mouth-blocking mechanism favored by a more constrained pore structure is likely occurring on mordenite.

Table 5
Estimated micropore volumes assuming hydrocarbon density of 0.8 g/cm^3

Sample	Estimated MPV (cm^3/g)	Sample	Estimated MPV (cm^3/g)
Y12S	0.19	Y12R	0.24
Y30S	0.25	Y30R	0.27
B18S	0.05	B18R	0.16
B25S	0.04	B25R	0.06
M20S	0.11	M20R	0.14

Querini and Roa [37] and Yoo et al. [34,39] have also compared the alkylation behavior of zeolite catalysts of various dimensionalities. Although their experimental conditions were different than the conditions applied here, both groups observed that zeolite pore structure played a role in catalyst deactivation. For example, beta outperformed other zeolites both in olefin conversion and selectivity to TMPs, and catalysts with one-dimensional (1D) pore structure [37] or cavities [34,39] deactivated faster.

If the density of the hydrocarbon deposits were known, then the MPV could be calculated. But because density is not known, an estimate of MPV can be obtained by assuming that hydrocarbon deposits are as bulky as the 2,2,4-TMP as proposed previously [37]. Consequently, we estimated expected MPVs using a density of 0.8 g/cm^3, fresh catalyst MPVs (Table 2), and hydrocarbon contents (Table 3). The results are given in Table 5. Comparing these estimated MPVs with the experimental results in Table 2, it is apparent that all estimated MPVs were higher. Although some pore plugging occurred on all samples, it occurred preferentially on the mordenite catalyst.

The DRIFTS spectra of all fully deactivated samples showed that aliphatic hydrocarbons are the major component of the species remaining on the used catalysts. Red shifts in zeolite framework vibrations around 1330–1360 cm^{-1} (not shown) were in agreement with hydrocarbon contents. The disappearance of hydroxyl bands on most spectra of spent catalysts indicates the interaction of adsorbed hydrocarbons with the internal surface of the zeolite catalysts. The hydrocarbons remaining on spent Y's (Figs. 3 and 4) and mordenite (Fig. 7) were branched aliphatic species. The formation of nonaromatic coke on the Y catalyst samples is in agreement with results reported by Stocker et al. [40] for protonated faujasite alkylation catalysts. With respect to both spent beta zeolite catalysts (Figs. 5 and 6), the important contribution of the CH_2 stretching peak around 2929 cm^{-1} revealed the presence of aliphatic hydrocarbons that were less branched than those shown on spent Y zeolite catalysts.

DRIFTS bands ascribed to highly unsaturated species were absent on most spectra of spent catalysts. Unsaturated species, such as alkenyl carbocations, were seen by DRIFTS only on spent beta zeolite catalysts and hydrogen deficient deposits possibly on Y12S (Fig. 3b).

UV–vis spectroscopy is more adequate than DRIFTS for examining adsorbed unsaturated hydrocarbons. Thus allylic and dienylic carbocations were seen by UV–vis on the Y12S catalyst (Fig. 8); Y30S showed a negligible contribution of such species (Fig. 9). In contrast, a significant contribution of allylic carbocations is seen on B18S (Fig. 10), B25S (Fig. 11), and M20S (Fig. 12) samples. The presence of unsaturated cyclic compounds was uncertain on the M20S sample, because the broad absorption band around 456 nm (curve M20S on Fig. 12) assigned to polyenylic carbocations may have overlapped unsaturated cyclic compounds absorbing around 430 nm.

In brief, Y zeolites were probably deactivated by a site-blocking mechanism produced mostly by adsorbed branched aliphatic hydrocarbons and small amounts of unsaturated species. A minor contribution of pore blockage cannot be completely ruled out. The total amount of hydrocarbons retained during reaction was relatively small, and these samples still maintained significant available micropore volume even when fully deactivated.

On average, beta zeolite catalysts displayed the best performances among all samples studied here. Similar to Y zeolite catalysts, higher SiO_2/Al_2O_3 ratio produced lower olefin conversion and TMP production. The total amounts of hydrocarbons retained were the highest among all samples investigated. When fully deactivated, the channel network of these catalysts was almost completely filled with hydrocarbon species, typically aliphatic hydrocarbons and small amounts of species with low degrees of unsaturation. As found in Y zeolite catalysts, some contribution of adsorbed hydrocarbons to pore blockage may be present.

Mordenite was the less attractive catalyst under the conditions applied in this study. A fully blocked pore system was displayed by the completely deactivated mordenite sample.

4.2. Removal of hydrocarbons by supercritical isobutane treatment

Once the nature of hydrocarbons remaining on spent catalysts is analyzed, a more detailed study of the effect of SFR on hydrocarbon removal can be undertaken. Zeolite pore structure plays an important role not only in hydrocarbon deposition, but also in hydrocarbon transformation and removal by supercritical isobutane treatment, as discussed below.

SFR was effective in recovering MPV in B18 and both Y zeolite catalysts, as can be easily seen by comparing the MPVs of treated and fresh samples (Table 2). This was not the case for B25 and M20 zeolite catalysts, in which negligible MPV was recovered and relatively small amounts of hydrocarbons were removed (Table 3) by SFR. For example, SFR changed the amount of hydrocarbons adsorbed on mordenite from 5.9 to 3.2%; however, a similar final hydrocarbon content (i.e., 2.6%) was found in B18 despite its initial higher hydrocarbon content (i.e., 11.5%).

The temperature ranges at which hydrocarbons desorbed from the catalysts during the TPO experiments might indicate a general trend toward “softer” hydrocarbons after SFR. However, the amount of hydrocarbons remaining on the catalysts was lower after SFR, and, consequently, the hydrocarbons are less diffusionally limited in exiting the catalyst micropores.

Comparing the differences between estimated (Table 5) and experimental (Table 2) MPVs, Y zeolite catalysts submitted to SFR displayed MPVs consistent with their amount of hydrocarbons. Although hydrocarbons remaining on the catalysts after SFR would not be expected to be as bulky as 2,2,4-TMP, this analysis provides some insight into general trends. Beta zeolite catalysts submitted to SFR exhibited MPVs around 50–60% of their estimates based on hydrocarbon content. For example, B18R was expected to display a MPV of 0.16 cm^3/g, whereas the experimental result was 0.10 cm^3/g. Although the hydrocarbon content of the beta and mordenite zeolite catalysts after SFR was lower than before SFR, slightly higher differences were found between the estimated and experimental MPVs. These results may be explained by the greater contribution of hydrocarbon deposits to pore plugging after SFR. The portion of hydrocarbons that did not desorb during SFR increased their molecular size and blocked some of the zeolite micropores. The almost complete MPV recovery on Y zeolite catalysts may be explained by the initial lower hydrocarbon content, high MPV of spent samples, and favorable open pore structure.

In contrast, two spent catalyst samples such as B18S and B25S, which displayed comparable amounts of hydrocarbons (Table 3) and comparable DRIFTS (Figs. 5 and 6) and UV–vis spectra (Figs. 10 and 11) before SFR, achieved very different nitrogen physisorption capacities after SFR treatment (B18R and B25R in Table 2). Whereas B18 recovered more than 50% of its fresh MPV and the amount of hydrocarbons retained decreased from 11.5 to 2.6%, B25 did not recover any significant nitrogen physisorption capacity and had a relatively small hydrocarbon content change, from 10.0 to 8.4%. These results suggest that the acid site density likely plays a role in the SFR process. Higher acid site densities may facilitate hydrogen transfer between isobutane and adsorbed hydrocarbons to react and desorb deposits from the catalyst surface. In contrast, lower acid site densities that involve higher acid strength of particular sites may retain hydrocarbons more strongly and hence will be more difficult to remove by the supercritical fluid.

DRIFTS analyses after SFR revealed highly unsaturated hydrocarbon bands with some degree of intensity on Y12R and weaker intensity on Y30R and B18R samples. Y samples (Figs. 3 and 4) showed a coke band around 1590 cm^{-1} and small contribution of aliphatic species. According to the TPO results, the hydrocarbon deposits on the Y12R were

0.0%; however, DRIFTS and the UV–vis spectra clearly indicated the presence of hydrocarbons. This discrepancy may be explained by the fact that DRIFTS and UV–vis analyses were performed on samples without any special pretreatment, whereas the TPO results were calculated after subtracting the weight changes of blank experiments (i.e., contacted with pressurized isobutane), which accounted for water contribution but may have masked minute amounts of hydrocarbons.

With respect to beta samples (Figs. 5 and 6), aliphatic hydrocarbons and alkenyl carbocations are demonstrated by their infrared spectra after SFR. Although the DRIFTS measurements are not intended to provide quantitative information on the amount of hydrocarbon deposits, the higher intensity of CH stretching vibrations shown in the B18R and B25R samples compared with the Y12R and Y30R samples is in agreement with the former samples' higher hydrocarbon content. A very small contribution of highly H-deficient deposits at 1568 cm^{-1} on the B18R spectrum was also seen. Some increase in branching on both beta zeolite catalysts was seen after SFR because of the increased intensity of the 2956 cm^{-1} band. Although the reaction to deactivate the catalysts was performed at 333 K, SFR occurred at a higher temperature (i.e., 453 K), which may have contributed to the increase in hydrocarbon branching. Increasing hydrocarbon branching with increasing temperature has been reported for other hydrocarbon reactions on zeolite catalysts [41]. With respect to M20R, DRIFTS analyses after SFR treatment revealed only the presence of highly branched aliphatic species (Fig. 7).

DRIFTS analyses after SFR also revealed completely recovered hydroxyl stretching vibrations only on Y12R, the zeolite sample that displayed a negligible amount of hydrocarbons after SFR. Furthermore, zeolite framework vibrations around 1330–1360 cm^{-1} (not shown) returned to their initial frequencies only on Y12R and Y30R samples, in agreement with their low hydrocarbon contents.

Unsaturated cyclic compounds had an important contribution on the UV–vis spectra of both Y samples submitted to SFR. This indicates that the presence of zeolite cavities favored cyclization/condensation reactions during SFR. In addition, monoenylic carbocations were seen in the SFR-treated betas and mordenite samples, and polyenylic carbocations were seen in the M20R sample.

In summary, submitting spent Y zeolite catalysts to SFR achieved an almost complete removal of hydrocarbon deposits and complete recovery of MPV. During SFR, small amounts of hydrocarbons underwent cyclization and condensation reactions to produce highly unsaturated cyclic species that remained on the catalyst channels after SFR.

The behavior of the beta zeolite catalysts during SFR confirmed the reactive nature of the SFR process. Submitting these catalysts to SFR made hydrocarbon removal greatly affected by the zeolite SiO_2/Al_2O_3 ratio. In the beta zeolite catalyst sample with higher acid site density, more than 50% of the fresh MPV was recovered and more than 75% of the hydrocarbon content removed by SFR. In the sample with lower acid site density, about 15% of its hydrocarbon content was removed by SFR, but this decrease did not produce MPV recovery. The hydrocarbon species remaining after SFR were mostly aliphatic hydrocarbons that underwent increased branching during SFR. Formation of some unsaturated cyclic species may have also occurred, mostly on the beta catalyst sample with higher acid site density. The bulkier nature of the adsorbed hydrocarbons remaining after SFR may contribute to significant pore plugging seen after SFR.

The picture for mordenite after SFR is a pore system that is almost fully blocked by carbonaceous deposits and has internal regions that are perhaps still active but unavailable to reactants. Although the SFR removed a portion of hydrocarbons remaining on the spent mordenite catalyst, this did not provide any important increase in MPV.

Zeolite pore structures that favor the formation of unsaturated cyclic species either during reaction or SFR are expected to have a less efficient catalyst activity recovery in the long term. The results given in Table 4 confirm this supposition. The faster activity decrease of the USY sample compared with the B18 sample resulted from the more condensed nature of hydrocarbons adsorbed on USY after SFR. B18 did not show an important contribution of condensed hydrocarbons after its first reaction/SFR cycle, which allowed for relatively more stable behavior when submitted to repeated reaction/SFR cycles.

5. Conclusions

Zeolite pore structure plays an important role in both hydrocarbon deposition and hydrocarbon transformation and removal by supercritical isobutane treatment. Even though most of the coke was removed in some catalysts, the DRIFTS profiles showed signals corresponding to hydrocarbons remaining on all of the catalysts after SFR treatment. During SFR, the formation of unsaturated cyclic or polycyclic compounds was hindered on beta zeolites and favored on Y zeolite catalysts, which present periodic expansions in pore structure. These hydrocarbon deposits are expected to have a toxic effect on catalyst activity recovery and to affect long-term catalyst activity after cyclic alkylation/SFR treatments.

Cyclic reaction/SFR experiments done to compare the longer-term performance of USY and beta zeolite samples demonstrated that neither catalyst recovered its initial performance after SFR. Moreover, both samples exhibited a continuous decrease in activity. The slower activity decrease in the beta sample may be ascribed to the hindered formation of toxic unsaturated cyclic or polycyclic hydrocarbons.

This suggests that betas with high acid site density may be the most appropriate zeolites for repeated reaction/SFR cycles. In contrast, zeolite catalysts with 1D pore structures,

such as mordenites, are likely not good candidates for SFR, because of diffusional limitations.

Acknowledgments

This research was supported through the INL Laboratory Directed Research and Development Program under DOE Idaho Operations Office Contract DE-AC07-99ID13727. The authors thank Joseph L. Rodriguez for contributing to the experimental work during his internship at INL. The valuable comments made by the editor and the reviewers are also gratefully acknowledged, but of course the authors alone are responsible for any deficiencies that may persist.

References

[1] A. Corma, A. Martinez, Catal. Rev.-Sci. Eng. 35 (1993) 483.
[2] M.C. Clark, B. Subramaniam, Ind. Eng. Chem. Res. 37 (1998) 1243.
[3] B. Subramaniam, V. Arunajatesan, C. Lyon, in: B. Delmon, G.F. Froment (Eds.), Stud. Surf. Sci. Catal., vol. 126, Elsevier, Amsterdam, 1999, p. 63.
[4] B. Subramaniam, Appl. Catal. A 212 (2001) 199.
[5] A.S. Chellappa, R.C. Miller, W.J. Thomson, Appl. Catal. A 209 (2001) 359.
[6] D.M. Ginosar, D.N. Thompson, K. Coates, D.J. Zalewski, Ind. Eng. Chem. Res. 41 (2002) 2864.
[7] D.M. Ginosar, K. Coates, D.N. Thompson, Ind. Eng. Chem. Res. 41 (2002) 6537.
[8] D.M. Ginosar, D.N. Thompson, K. Coates, D.J. Zalewski, R.V. Fox, US Patent 6,579,821 (2003), to Bechtel Bwxt Idaho, LLC.
[9] D.N. Thompson, D.M. Ginosar, K. Coates, Abstr. Pap. Am. Chem. Soc. 222 (2001) U466.
[10] D.M. Ginosar, D.N. Thompson, K.C. Burch, Appl. Catal. A 262 (2004) 223.
[11] L.M. Petkovic, D.M. Ginosar, Appl. Catal. A 275 (2004) 235.
[12] D.N. Thompson, D.M. Ginosar, K.C. Burch, Appl. Catal. A 279 (2005) 109.
[13] D.M. Bibby, R.F. Howe, G.D. McLellan, Appl. Catal. A 93 (1992) 1.
[14] S. Brunauer, P.H. Emmet, E. Teller, J. Am. Chem. Soc. 60 (1938) 309.
[15] B.C. Lippens, J.H. de Boer, J. Catal. 4 (1965) 319.
[16] R.J. Taylor, D.E. Sherwood, Appl. Catal. A 155 (1997) 195.
[17] R.A. Nyquist, The Interpretation of Vapor Phase Infrared Spectra, Sadtler Research Laboratories, Philadelphia, PA, 1984, p. 71.
[18] A. Corma, A. Martinez, C. Martinez, Appl. Catal. A 134 (1996) 169.
[19] M.A. Makarova, A.F. Ojo, K. Karim, M. Hunger, J. Dwyer, J. Phys. Chem. 98 (1994) 3619.
[20] A. Jentys, J.A. Lercher, in: H. van Bekkum, E.M. Flanigen, P.A. Jacobs, J.C. Jansen (Eds.), Introduction to Zeolite Science and Practice, Elsevier, Amsterdam, 2001, p. 345.
[21] L. Bertsch, H.W. Habgood, J. Phys. Chem. 67 (1963) 1621.
[22] S.M.C. Menezes, V.L. Camorim, Y.L. Lam, R.A.S. San Gil, A. Bailly, J.P. Amoureux, Appl. Catal. A 207 (2001) 367.
[23] H.G. Karge, W. Niessen, H. Bludau, Appl. Catal. A 146 (1996) 339.
[24] P.J. Kunkeler, B.J. Zuurdeeg, J.C. van der Waal, J.A. van Bokhoven, D.C. Koningsberger, H. van Bekkum, J. Catal. 180 (1998) 234.
[25] S.W. Yang, J.N. Kondo, K. Domen, Catal. Today 73 (2002) 113.
[26] I. Kiricsi, H. Forster, G. Tasi, J.B. Nagy, Chem. Rev. 99 (1999) 2085.
[27] A. Feller, J.O. Barth, A. Guzman, I. Zuazo, J.A. Lercher, J. Catal. 220 (2003) 192.
[28] F.R. Chen, G. Coudurier, J.F. Joly, J.C. Vedrine, J. Catal. 143 (1993) 616.
[29] D. Spilbauer, G.A.H. Mekhemer, E. Bosch, H. Knözinger, Catal. Lett. 36 (1996) 59.
[30] H. Förster, J. Seebode, P. Fejes, I. Kiricsi, J. Chem. Soc. Faraday Trans. 83 (1987) 1109.
[31] I. Kiricsi, C. Flego, G. Bellussi, Appl. Catal. A 126 (1995) 401.
[32] C. Pazè, B. Sazak, A. Zecchina, J. Dwyer, J. Phys. Chem. B 103 (1999) 9978.
[33] H.G. Karge, M. Laniecki, M. Ziolek, G. Onyestyak, A. Kiss, P. Kleinschmit, M. Siray, in: P.A. Jacobs, R.A. Van Santen (Eds.), Stud. Surf. Sci. Catal., vol. 49, Elsevier, Amsterdam, 1989, p. 1327.
[34] K. Yoo, E.C. Burckle, P.G. Smirniotis, J. Catal. 211 (2002) 6.
[35] V.B. Kazansky, in: P.A. Jacobs, N.I. Jaeger, P. Jiru, V.B. Kazansky, G. Schulz-Ekloff (Eds.), Stud. Surf. Sci. Catal., vol. 18, Elsevier, Amsterdam, 1984, p. 61.
[36] F. Tielens, W. Langenaeker, P. Geerlings, J. Mol. Struct.—Theochem. 496 (2000) 153.
[37] C.A. Querini, E. Roa, Appl. Catal. A 163 (1997) 199.
[38] Y. Zhuang, F.T.T. Ng, Appl. Catal. A 190 (2000) 137.
[39] K. Yoo, E.C. Burckle, P.G. Smirniotis, Catal. Lett. 74 (2001) 85.
[40] M. Stocker, H. Mostad, T. Rorvik, Catal. Lett. 28 (1994) 203.
[41] J.P. Lange, A. Gutsze, H.G. Karge, J. Catal. 114 (1988) 136.